nature materials

ARTICLES

PUBLISHED ONLINE: 30 OCTOBER 2017 | DOI: 10.1038/NMAT5021

Additively manufactured hierarchical stainless steels with high strength and ductility

Y. Morris Wang[1]*, Thomas Voisin[1], Joseph T. McKeown[1], Jianchao Ye[1], Nicholas P. Calta[1], Zan Li[1], Zhi Zeng[2], Yin Zhang[2], Wen Chen[3], Tien Tran Roehling[1], Ryan T. Ott[4], Melissa K. Santala[5], Philip J. Depond[1], Manyalibo J. Matthews[1], Alex V. Hamza[1] and Ting Zhu[2]

Many traditional approaches for strengthening steels typically come at the expense of useful ductility, a dilemma known as strength–ductility trade-off. New metallurgical processing might offer the possibility of overcoming this. Here we report that austenitic 316L stainless steels additively manufactured via a laser powder-bed-fusion technique exhibit a combination of yield strength and tensile ductility that surpasses that of conventional 316L steels. High strength is attributed to solidification-enabled cellular structures, low-angle grain boundaries, and dislocations formed during manufacturing, while high uniform elongation correlates to a steady and progressive work-hardening mechanism regulated by a hierarchically heterogeneous microstructure, with length scales spanning nearly six orders of magnitude. In addition, solute segregation along cellular walls and low-angle grain boundaries can enhance dislocation pinning and promote twinning. This work demonstrates the potential of additive manufacturing to create alloys with unique microstructures and high performance for structural applications.

Making lighter, stronger, and more ductile materials has been a central focus of materials scientists and engineers[1–8]. One longstanding challenge, however, is to overcome the strength–ductility trade-off that exists ubiquitously in pure metals and alloys[9,10], which hampers their structural applications. Austenitic 316L stainless steel (SS), in particular, is a workhorse material of our society owing to its excellent corrosion and oxidation resistance, and is used in such diverse applications as kitchen tools, medical implants, oil rigs, and nuclear power plants. One major drawback of coarse-grained 316L SS is its low yield strength (~250–300 MPa) (ref. 11). Many traditional metallurgical routes to strengthening this material (for example, cold rolling, forging) inevitably lead to a severe drop in useful tensile ductility. To date, the strategies to achieve both high strength and ductility remain rare despite decades of studies.

Recently, several engineered gradient microstructures with spatial variations of either grain size or twin spacing have been demonstrated to have the potential of achieving both high strength and high ductility[10,12,13]. However, nearly all these approaches require tooling or surface mechanical treatment, which are not readily applicable to the complex geometry components necessary for practical applications. Here we apply a laser powder-bed-fusion (L-PBF) technique for additive manufacturing (AM)[14,15] to produce 316L SS with an exceptional combination of strength and ductility. Unlike any conventional synthesis/manufacturing technique, L-PBF 'prints' materials and parts directly from a computer-aided design file, and thus offers unique advantages of design freedom for complex geometry without the need for tooling. As L-PBF is a layer-by-layer build technology, it permits ample opportunities to tailor the microstructure and subsequent mechanical properties. The highly localized melting, strong temperature gradient[16], and high solidification front velocity associated with L-PBF processes generate extremely nonequilibrium microstructures that are not accessible through conventional methods. In essence, L-PBF integrates materials synthesis and manufacturing in a single print, making it attractive for a broad range of technological applications.

A fundamental understanding of the structure–property relationship in AM metals is critical to this disruptive technology. One challenge for L-PBF processes is to optimize a set of laser processing parameters so as to produce high-quality, porosity-free samples. To this end, we have used a combined approach of modelling and experiments[17] to identify the laser parameters and build near fully dense (>99.2%) square pillars and rectangular plates of 316L SS (Methods and Supplementary Table 1). Two different types of L-PBF machines were used and named as 'Concept' and 'Fraunhofer', respectively. Supplementary Table 2 lists the typical composition of 316L SS fabricated by L-PBF from each machine, together with a reference AISI 316L sample[11]. The overall composition of our L-PBF 316L SS is similar to that of the commercial AISI 316L SS except for the oxygen and nitrogen contents. Both impurities could originate from the powder source, which was atomized in a nitrogen environment. Synchrotron X-ray diffraction (SXRD) indicates that the primary phase in as-built 316L SS is face-centred cubic, with no measurable body-centred cubic phase present (Supplementary Fig. 1).

Microstructure characterization (Methods) of an as-built Concept sample reveals multiple length scales and chemical heterogeneity, as schematically illustrated in Fig. 1a. The grain orientation and size distribution were measured by electron backscatter diffraction (EBSD) in a scanning electron microscope (SEM) (Fig. 1b,f). Grains under EBSD exhibit a ripple pattern instead of a traditional faceted morphology. A continuous change of colour and thus orientation was frequently observed within one single grain. Overall, the microstructure of L-PBF 316L SS shows a

[1]Materials Science Division, Lawrence Livermore National Laboratory, Livermore, California 94550, USA. [2]Woodruff School of Mechanical Engineering, Georgia Institute of Technology, Atlanta, Georgia 30332, USA. [3]Materials Engineering Division, Lawrence Livermore National Laboratory, Livermore, California 94550, USA. [4]Division of Materials Sciences and Engineering, Ames Laboratory (USDOE), Ames, Iowa 50011, USA. [5]School of Mechanical, Industrial and Manufacturing Engineering, Oregon State University, Corvallis, Oregon 97331, USA. *e-mail: ymwang@llnl.gov

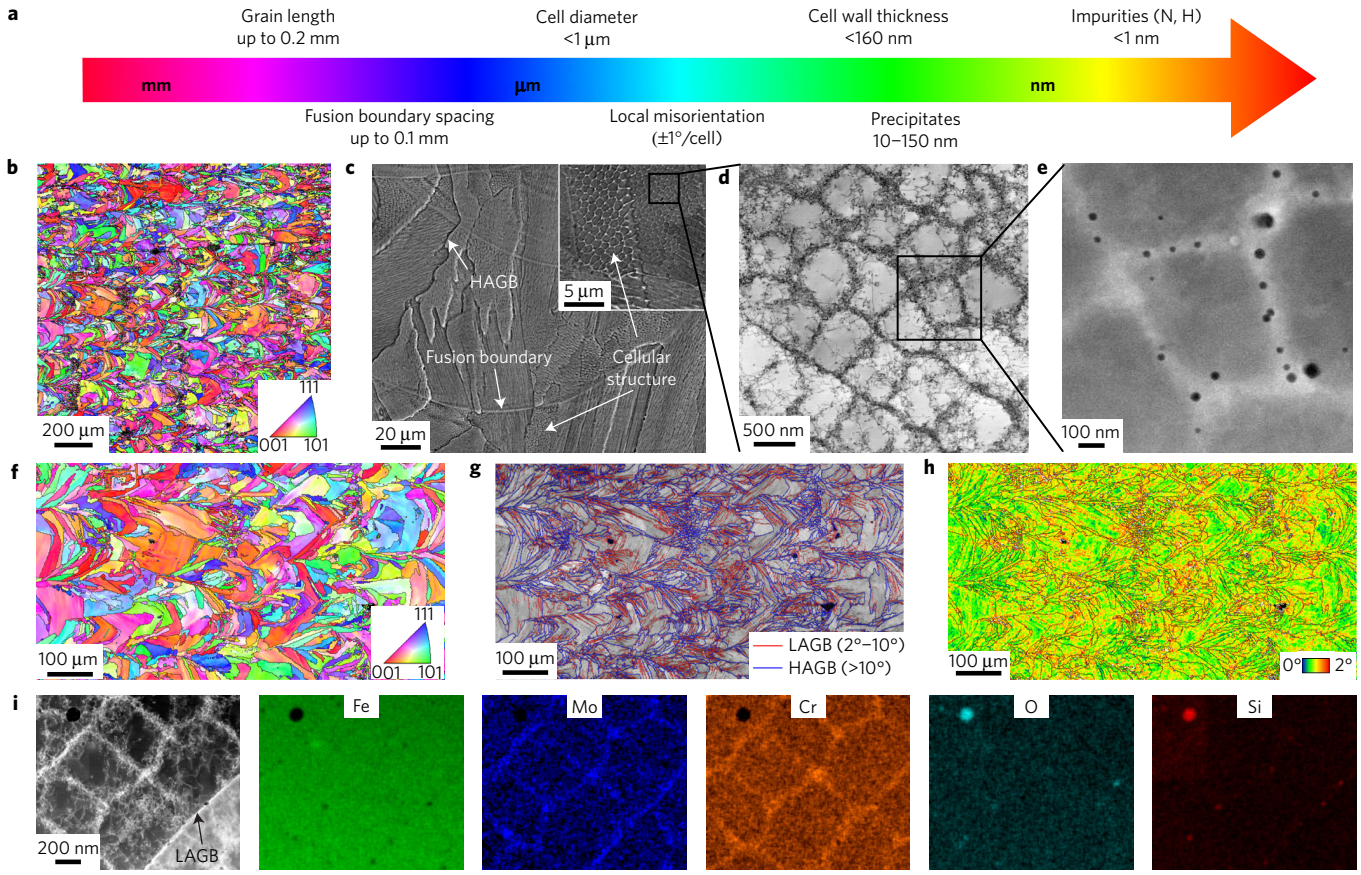

Figure 1 | Typical microstructure of a laser powder-bed-fusion (L-PBF) produced 316L stainless steel (SS). a, A schematic of various length scales uncovered in L-PBF 316L SS. **b**, A cross-sectional electron backscatter diffraction (EBSD) inverse-pole figure (IPF) map of the as-built L-PBF 316L SS sample showing grain orientations. The IPF map was acquired with a 2-μm step size. The build direction is horizontal. **c**, A cross-sectional scanning electron microscopy (SEM) image, revealing fusion boundaries, high-angle grain boundaries (HAGBs), and solidification cellular structures. The inset shows the cellular structure at a higher magnification. The build direction in this image is vertical. **d**, A bright-field transmission electron microscopy (TEM) image of solidification cells. **e**, A high-angle annular dark-field (HAADF) scanning TEM (STEM) image of the solidification cells shown in **d**. The nanoparticles segregated to the cell walls were identified as transition-metal-rich silicates formed during L-PBF processing. **f**, EBSD IPF map acquired with a 1-μm step size. **g**, EBSD image quality (IQ) map with HAGBs and low-angle grain boundaries (LAGBs) superimposed. As indicated in the legend, HAGBs (>10°) are coloured blue and LAGBs (2°–10°) are coloured red. The fraction of HAGBs and LAGBs are ~59% and ~41%, respectively. **h**, A map of the kernel average misorientation (KAM), measured in degrees, to illustrate the local misorientation across individual grain. It is evident that all of the grains have local misorientations on the order of 0.5°–1°. **i**, A HAADF STEM (Z contrast) image showing segregation of Mo and Cr to the solidification cellular walls and a LAGB, with corresponding Fe, Mo, and Cr energy-dispersive spectroscopy (EDS) maps that confirm this segregation. The EDS map also verifies that particles are mostly rich with Si, O, and Mn (see Supplementary Fig. 3).

highly nonconventional grain shape, distribution, and orientation gradient. Our EBSD measurements further indicate that L-PBF 316L SS contains a large fraction of low-angle grain boundaries (LAGBs, 2°–10°, ~41% of the total GBs, Fig. 1g). Orientation gradients or local misorientations across grains are observed, as evidenced in the kernel average misorientation (KAM) map shown in Fig. 1h, where the angular orientation deviation from pixel to pixel inside each individual grain is mapped. A comparison of Fig. 1g and h indicates that there is a direct correlation between orientation deviation and LAGBs. The estimated average grain size (d) based on the high-angle grain boundaries (HAGBs) is 45 ± 7.9 μm, with a large standard deviation, leading to a grain area distribution that spans several orders of magnitude (Supplementary Fig. 2). These EBSD data suggest that L-PBF 316L SS is an unconventional material with a broad grain-size distribution, a large fraction of LAGBs, and ripple-like grain shapes. Voids are also present but the volume fraction is far less than 1%.

Further microstructure characterization reveals a broad range of internal boundaries, subgrain structures, and chemical segregations. The as-built 316L SS has a highly heterogeneous microstructure, both structural and chemical (Fig. 1c–e), with fusion boundaries, dendritic and cellular walls, dislocations, precipitates, segregated elements (for example, Cr and Mo), and atomic scale impurities (for example, N and H) (Supplementary Table 2). The microstructural length scales span five to six orders of magnitude, from nanometre to sub-millimetre, in contrast to conventional counterparts. Twins are not observed in the as-built materials. Of particular interest is the solidification cellular structures that are commonly observed in L-PBF alloys. The size of these cellular structures in our materials is less than 1 μm (Fig. 1d) (that is, substantially smaller than $d \sim 45 \pm 7.9$ μm). The volume fraction and size of the cellular structures vary from sample to sample, in agreement with previous reports[18]. Our compositional mapping reveals segregation of Cr and Mo along the walls of solidification cellular structures and LAGBs (Fig. 1i). The precipitates of transition-metal-rich silicates (in which Mn and Cr content varies from particle to particle) with sizes in the range 10–150 nm are also observed along the cellular walls (Fig. 1e and Supplementary Fig. 3). Cellular walls are observed to be decorated with a high density of dislocations (Fig. 1d), with relatively

clean interiors (Fig. 1i, see the high-angle annular dark-field (HAADF) image). The size and wall thickness of these solidification cells are known to be connected to solidification conditions (that is, thermal gradient, cooling rate, solidification front velocity) during the L-PBF processes[19]. In our case, the wall thickness is typically <160 nm. The cellular structures have been commonly reported in Al-based, Co-based, and Fe-based alloys produced by L-PBF processing[19]. Because of the distinct compositional difference between the walls and the matrix, secondary phases have sometimes been reported for these walls. Therefore, these solidification cellular structures are not conventional dislocation walls despite their morphological similarity.

Interestingly, our transmission electron microscopy (TEM) studies reveal substantially less or little elemental segregation in the Fraunhofer sample (Supplementary Fig. 4), suggesting that the elemental segregation and cellular structures are closely related to the laser processing parameters. To qualitatively compare various processing parameter effects on microstructures, in Supplementary Fig. 5 we construct a normalized processing diagram for our L-PBF materials, following the normalized equivalent energy density (E_0^*) approach (Methods)[20,21]. Although relatively crude, the E_0^* diagram helps to delineate the useful processing windows and major microstructure length scales involved in this work. In general, we employ combinations of laser parameters that fall near the $E_0^* \sim 2$ isopleth line for the Concept machine and $8 < E_0^* < 16$ for the Fraunhofer machine, respectively; that is, the latter employs a much higher energy efficient process by applying a significantly larger beam size (and thus wider melt pool), compensated by the slower laser speed and greater build layer thickness.

Tensile tests of as-built samples from two different types of machines indicate that L-PBF 316L SS has high yield strengths, which are two to three times stronger than those of as-cast, as-wrought, and coarse-grained counterparts[11] (Fig. 2a). In addition, L-PBF materials also show a large tensile elongation to failure. Of particular significance is that L-PBF 316L SS shows a steady strain-hardening ability at high stress levels, as indicated by the Kocks–Mecking plot shown in Supplementary Fig. 6, leading to a uniform tensile elongation that well surpasses the conventional 316L SS with similar strengths (Fig. 2b and Supplementary Table 3). This exceptional combination of yield strength and uniform tensile elongation is seen in a series of L-PBF 316L SS samples printed by different laser processing parameters, far outside 'the crescent-shaped domains' enclosing the inversely related strength and ductility data for 316L SS reported in the literature[11,22–31]. Notably, the L-PBF material even surpasses those high-performance 316L SS, including materials strengthened by nanotwin bundles[11] and those with bimodal grain structures[32].

An increased strength is commonly reported for several L-PBF metals and alloys[14,33–41], including L-PBF 316L SS[34,35,41–43]. However, this phenomenon is not well understood and has often been attributed to a single strengthening source such as solidification cellular walls[44], dislocations[34], microstructure refinement[45], or nanoprecipitates[41]. In particular, the average diameter of solidification cells has been previously applied to scale the strength of L-PBF 316L SS[18,35,44]. Based on a series of SEM images similar to the one shown in the inset of Fig. 1c, we measured average solidification cell sizes of 0.58 ± 0.07 μm and 0.93 ± 0.04 μm, respectively, for the Concept sample (red curve in Fig. 2a) and the Fraunhofer sample (blue curve in Fig. 2a). Assuming a Hall–Petch-type strengthening behaviour, where the yield strength σ_y scales with the cell size (L_c): $\sigma_y = 183.31 + 253.66/\sqrt{L_c}$ (MPa) (Supplementary Fig. 7), we calculate σ_y values of 516 MPa and 446 MPa, respectively. These values account for a substantial portion of the measured yield strengths of 590 ± 5 MPa and 450 ± 10 MPa, suggesting that the solidification cellular structure is a major contributor to the strength. Interestingly, we also measured an approximately

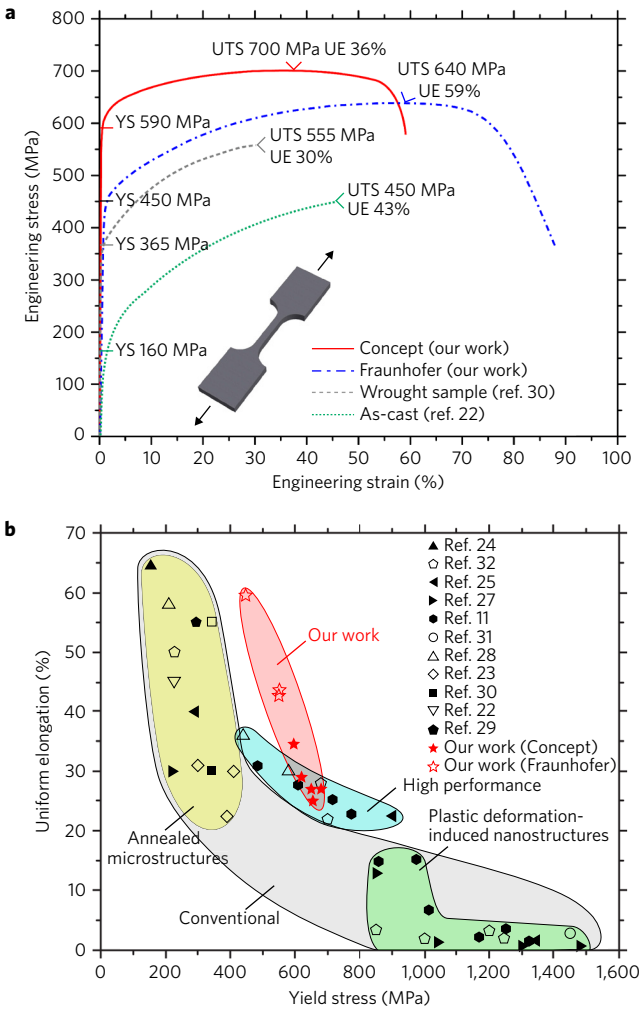

Figure 2 | Tensile properties of L-PBF 316L stainless steels (SS). **a**, Representative tensile engineering stress–strain curves for two L-PBF 316L SS (red curve: Concept sample; blue curve: Fraunhofer sample), compared to those of as-cast and as-wrought materials. The yield strength (YS), uniform elongation (UE), and ultimate tensile strength (UTS) are marked on the curves. **b**, A summary of yield stress versus uniform elongation for various 316L SS, including our work, high-performance materials (strengthened by nanotwin bundles and bimodal grain materials), conventional coarse-grained materials (annealed microstructures), and materials strengthened through traditional plastic deformation. The outstanding combination of strength and ductility observed in 3D-printed steels (our work) exceeds that of conventional and even high-performance 316L SS. The error bar of each data point from our work is shown in Supplementary Table 3.

48 ± 27% volume fraction of grains containing the solidification cellular structures in the Concept sample. The large error bar from the measurement is due to the large variations of cell volume fraction from image to image and the uncertainty in distinguishing between cellular structures and dendrites from the cross-section images. Additionally, questions remain whether the solidification cells can be as effective as HAGBs in terms of strengthening, in which cellular wall thickness is considered critical[46]. Nevertheless, this simplified estimate hints at additional strengthening effects of other sources such as dislocations and LAGBs in L-PBF 316L SS. Surprisingly, we measured $d \sim 20 \pm 4.0$ μm (Supplementary Fig. 8) for the Fraunhofer sample, which is substantially smaller than that (45 ± 7.9 μm) of the Concept sample. This is counterintuitive, as the former shows a much lower yield strength. This favourably

argues that the strength of L-PBF 316L SS is mainly determined by its subgrain structures instead of HAGBs. The strengthening effect of oxides is found to be negligibly small in our Concept samples (Supplementary Fig. 9).

To understand the origin of steady work-hardening behaviour of L-PBF 316L SS, we performed *in situ* SXRD experiments on three Concept samples, the main results of which are presented in Fig. 3 and Supplementary Figs 10–13. The high-energy synchrotron source (~100 keV) allows us to track six reflections in real time (namely, 111, 200, 220, 311, 222, 400) during tensile deformation (Supplementary Fig. 10). Figure 3a shows a tensile true stress–strain curve tested at a $2.0 \times 10^{-4}\ s^{-1}$ strain rate, with two unloading (U1, U2) and reloading (R1, R2) segments. A hysteresis loop associated with the Bauschinger effect is evident in the second unloading–reloading cycle, suggesting the existence of back stresses during plastic deformation (Supplementary Fig. 11). In heterogeneous materials the back stress has been reported to help strain hardening[13]. The residual stress has also been considered important in influencing the yield and work-hardening behaviour of some dual phase steels[47]. However, a similar residual stress effect is not anticipated here. In L-PBF 316L SS, the grain-level residual stress may not necessarily play a deterministic role, since the deformation is shown not to be dictated by the grain size. Instead, the residual stresses at the subgrain level may become important due to high heterogeneities and associated dislocations induced during processing. The residual stress effects warrant further study in L-PBF materials in the future.

To investigate the load partitioning and associated microplasticity, we calculate the elastic lattice strain as $\varepsilon^{hkl} = (d^{hkl} - d_0^{hkl})/d_0^{hkl}$, where d_0^{hkl} and d^{hkl} are lattice spacings for a crystallographic plane hkl at the stress-free state (see Methods) and during loading, respectively. The d_0^{hkl} values are obtained by measuring a stress-released 316L SS, and the reference elastic lattice strain (ε_r^{hkl}) is calculated according to $\varepsilon_r^{hkl} = \sigma/E^{hkl}$, where σ is the applied stress and E^{hkl} is the elastic modulus along a specific hkl direction (see Supplementary Table 4). Figure 3b displays the measured ε^{hkl} versus true stress along the loading direction for four representative orientations (see Supplementary Fig. 12 for the transverse direction), along with the reference ε_r^{hkl} to guide the eyes. In contrast to the well-annealed, coarse-grained material[48], the L-PBF 316L SS exhibits a strong nonlinear response of ε^{hkl} at the outset of loading. This nonlinear behaviour is due to anisotropic residual strains in the as-built samples, manifested by nonzero ε^{hkl} at the zero stress. This causes the deformation of L-PBF 316L SS to be highly heterogeneous in the initial loading. Interestingly, Fig. 3c indicates that ε^{hkl} becomes more linear during the second reloading (R2) until plastic yielding occurs at ~650 MPa. Similar to the coarse-grained materials, the two elastically softest reflections 200 and 311 remain the softest in the plastic region, and 222 and 220 reflections are the stiffest. These observations suggest a strong heterogeneous hardening behaviour during the initial loading and reloading, causing strain/stress repartitions and a change of internal stresses. The 222 texture evolution plots shown in Fig. 3d,e indicate the build-up of 222 texture along the loading direction, consistent with deformation mediated by dislocation slips. In addition, 70° grain reorientations also occur, suggestive of twinning activities[49]. Concurrently, a strong accumulation of defects is detected, as evidenced by the continuous 400 peak broadening during loading (Supplementary Fig. 13).

As suggested by our *in situ* SXRD studies, the strong heterogeneities, pre-existing defects and strains/stresses in as-built 316L SS have impacts on the deformation behaviour. Our post-mortem microstructural investigations at different strain levels in Fig. 4 reveal a variety of concurrent deformation mechanisms, including dislocation slips, cellular wall evolution, and deformation twinning. At a relatively low strain (~3%) (Fig. 4a–c), dislocation slip is the dominant deformation mechanism. At this strain level, the cellular size and shape remain unchanged (Fig. 4a), suggesting the pinning effects of segregated elements (that is, Cr and Mo). Dislocation trapping along the cellular walls is visible (inset of Fig. 4a). Also, one set of deformation twins is observed in a few grains (<10% of total grains) to nucleate from HAGBs and penetrate through the cellular walls and LAGBs (Fig. 4b). The average twin spacing at this stage is larger than 1 μm (Fig. 4c). The penetration of deformation twins across the cellular walls subdivides these cellular structures and promotes dislocation-twin and dislocation-cellular wall interactions, thus offering a progressive work-hardening mechanism.

To further investigate the role of the cellular structures on the plastic deformation and strain-hardening behaviour, we performed nanometre-resolution inverse-pole figure orientation mapping (IPFOM) in TEM for the 3%-deformed sample (Fig. 4d,e). In addition to little shape change of the cellular walls after deformation, surprisingly, we do not reveal any local misorientation across the majority of these walls (Fig. 4e). This confirms that these walls are not traditional dislocation walls that usually serve to accommodate local misorientations across the dislocation walls[50]. In contrast, our KAM map shown in Fig. 4d,e reveals an up to 1.5° misorientation inside the cells that is associated with geometrically necessary dislocations. This suggests a strong dislocation trapping and retention mechanism inside these walls, consistent with the observed strain-hardening behaviour. The dislocation blockage is also observed along the HAGBs (Fig. 4d, KAM map).

As the applied strain increases to ~12%, twinning becomes an important mechanism. Numerous events of different twin sets cross each other inside the same grain (Fig. 4f,g). The cellular structure is retained at this strain level but slightly elongated. Twin–twin and twin–cellular walls intersections provide a unique three-dimensional network for progressive and steady work hardening in L-PBF 316L SS that is not readily available in conventional counterparts. At an even higher strain level of ~36%, the twin density increases substantially (Supplementary Fig. 14). However, the cellular structure is retained; it continues to interact with deformation twins and forms a massive three-dimensional network obstacles to dislocation propagation. These post-mortem TEM studies indicate the key roles that solidification cells and deformation twins play in maintaining the steady work-hardening ability of L-PBF materials. In Fig. 2a, we observe that the high-strength L-PBF 316L SS has a low but steady work-hardening rate, probably due to the regulation effect of solidification cellular structure, which is relatively stable under deformation and helps to retain dislocations. In the meantime, deformation twinning progressively contributes to and further helps sustain the strain hardening at high stress levels, leading to a large uniform tensile elongation.

To understand the impact of experimentally observed hierarchical microstructures, we developed a size-dependent crystal plasticity finite element (CPFE) model (Methods) to investigate the effects of grain-level and subgrain-level heterogeneities and defects on the stress–strain responses. Although EBSD measurements revealed a broad distribution of grain sizes and grain areas, our d-dependent CPFE simulations (Supplementary Fig. 15a–c) indicate that the strength and strain hardening are not controlled by the length scale effect of EBSD-identified grains, which mostly involve HAGBs (>10°). Specifically, we constructed a polycrystal model (Supplementary Fig. 15a) with a wide distribution of d, and hence a grain area distribution similar to that of L-PBF 316L SS (Supplementary Figs 2 and 15b). We developed a d-dependent constitutive model, in which both σ_y and strain-hardening properties within each grain depend on the local grain size. The corresponding constitutive parameters were determined by fitting to the experimental data of 316L SS that closely follow the Hall–Petch equation between σ_y and d. Using this d-dependent CPFE model, we simulated the stress–strain response of uniaxial compression of L-PBF 316L SS. The numerical results show that σ_y and strain-hardening responses are much lower than those

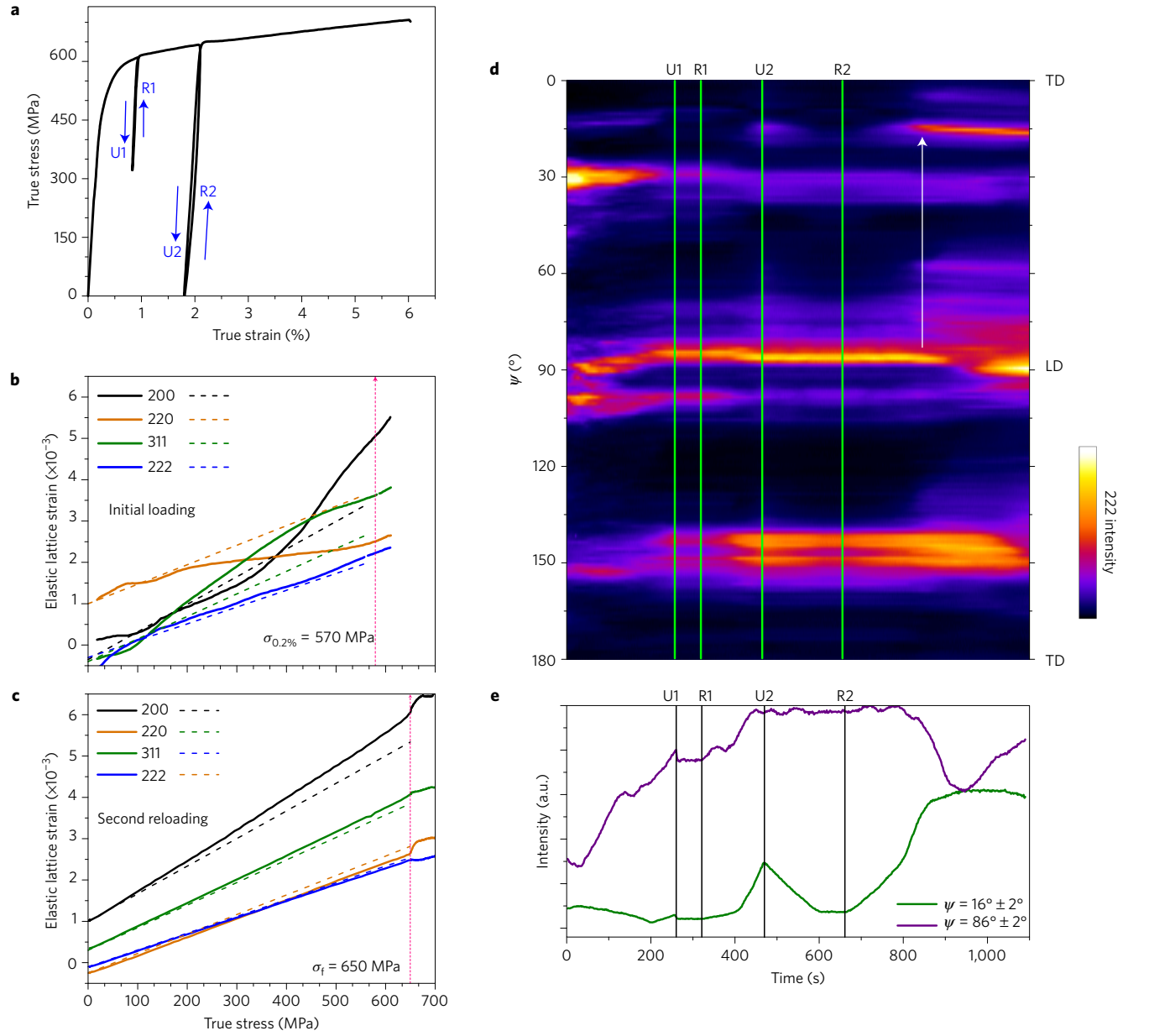

Figure 3 | Synchrotron X-ray diffraction (SXRD) measurements during tensile deformation of an L-PBF 316L SS. a, True stress–true strain curve for the *in situ* SXRD experiments, containing two unloading (U) and reloading (R) segments. The nominal strain rate was 2.0×10^{-4} s^{-1}. **b**, Elastic lattice strain (ε^{hkl}, solid lines) along the loading direction (LD) during the initial deformation, for four *hkl* indices (namely, 200, 220, 311, 222). The ε^{hkl} for 111 is not calculated due to the slight saturation of the detector for this peak. The dashed lines represent the reference lattice strain (ε_r^{hkl}) calculated on the basis of the elastic constant of each reflection. Note that the initial ε_r^{hkl} is shifted to better guide the eyes. A significant non-linear elastic strain behaviour is observed, suggestive of inhomogeneous deformation. The details of ε^{hkl} behaviour vary from sample to sample; but all samples exhibited nonlinear lattice strain evolution during the initial stage of loading. **c**, The ε^{hkl} behaviour during the second reloading (R2), showing much more linear elastic behaviour up to an applied stress of ~650 MPa, after which strong deviations from linearity are observed. **d**, Texture evolution of the 222 reflection during deformation, represented as diffracted intensity as a function of in-plane azimuthal angle (ψ) and testing time. The unloading and reloading are marked in green. The redistribution of residual strain observed in **b** also causes grain rotation at early test times. A clear build-up of 222 texture along the LD is observed, consistent with grain rotation due to dislocation slips, as well as 70° grain reorientations that agree with deformation twinning. One such reorientation is highlighted with a white arrow. **e**, The scattered intensity at two ψ angles related to the 70° grain reorientation highlighted in **d**. The change in scattered intensity corresponding to twin-induced grain reorientation begins at ~800 s.

from experimental measurements (see the green curve versus black curve in Supplementary Fig. 15c). This lends direct support to our earlier analysis of the important contributions of subgrain heterogeneities and defects to the strength and hardening of L-PBF 316L SS. To a first-order approximation, we assumed that an effective subgrain length scale (denoted as L) controls the strength and hardening of L-PBF 316L SS. That is, the yield strength obeys the aforementioned Hall–Petch equation through L instead of grain size, such that $\sigma_y = 183.31 + 253.66/\sqrt{L}$ (MPa), and the hardening parameters are also modified accordingly. The simulated stress–strain response (see the red curve in Supplementary Fig. 15c) closely matches the experimental measurement. The extracted L value is ~205 nm. This result reinforces the notion that the strength, hardening and ductility of L-PBF SS are controlled by the

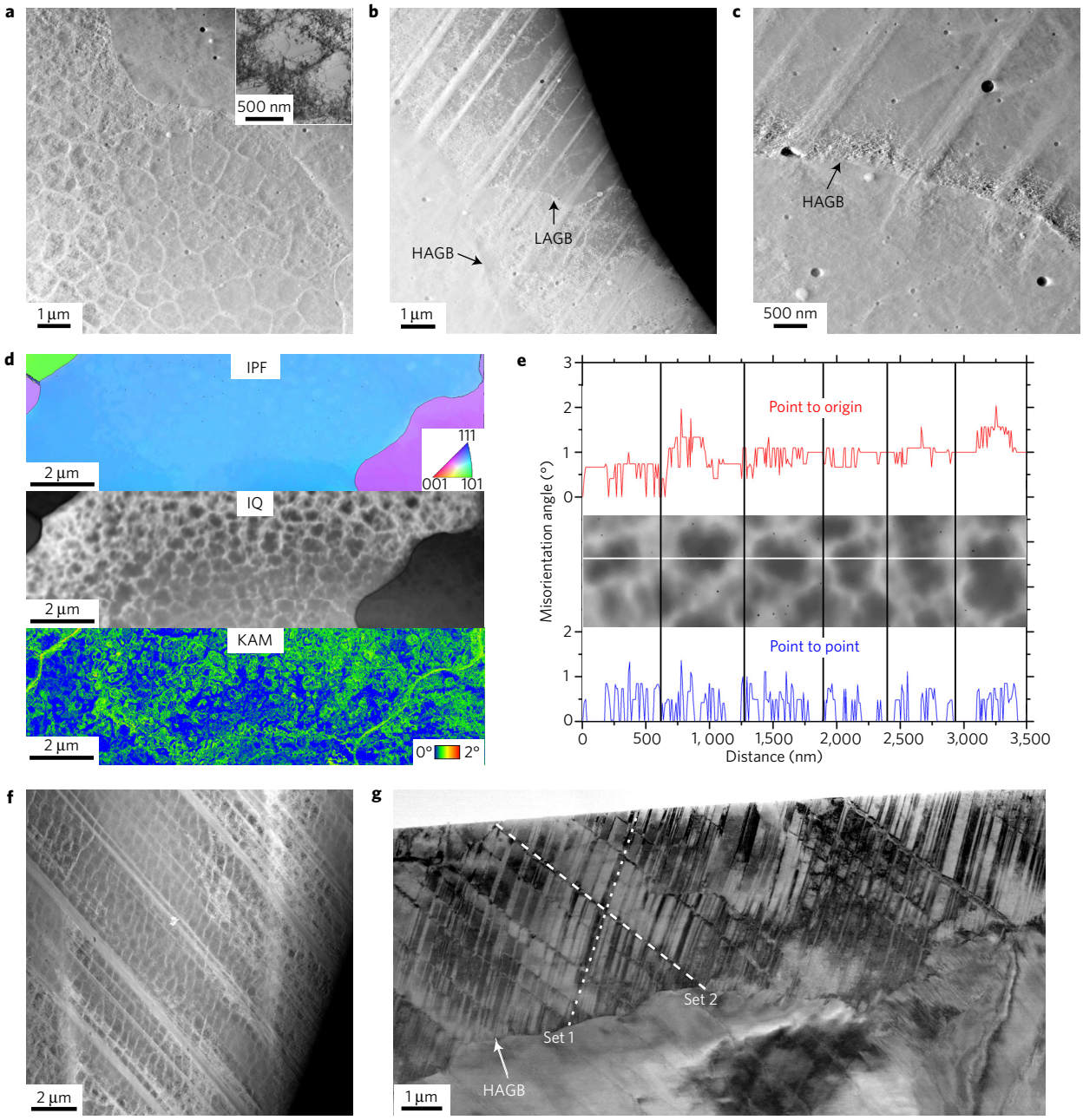

Figure 4 | Deformation structures of an L-PBF 316L SS after different levels of strain. a–c, Representative deformation microstructures at ~3% tensile strain. **a**, A HAADF STEM image of a solidification cellular structures after deformation. The shape and size of the cells are little changed. Trapping of dislocations at the cell walls was observed (inset). **b**, Deformation twins appear to nucleate from a HAGB and propagate through the cellular walls and a LAGB. **c**, A magnified image of **b**, showing that the deformation twin spacing is typically larger than 1 μm. **d**, Inverse-pole figure (IPF, top panel) map acquired from a solidification cell region after 3% strain, with associated IQ (middle panel) and KAM (bottom panel) maps. The data was acquired using precession electron diffraction (PED)–based automated crystal orientation mapping (ACOM) in the TEM with a 10-nm beam size and a 10-nm step size. **e**, Plots of the misorientation angle variation, measured both with respect to the origin and from point to point, across multiple cells of the cellular solidification structure after ~3% strain, indicated by the solid white line in the image. **f**,**g**, Deformation microstructures at ~12% tensile strain. **f**, A HAADF STEM image showing intersections of deformation twins with the walls of solidification cells. These cells are observed to be slightly elongated at this strain. **g**, A bright-field TEM image revealing the intersections of twins (labelled as Set 1 and Set 2 in the upper grain of the image). The arrow indicates the intersection of twins with a HAGB, suggesting that HAGBs are the nucleation and/or blockage sites for twinning.

collective effect of hierarchically heterogeneous microstructures, instead of the grains with HAGBs or a single length scale associated with subgrain solidification cellular structures (see the corresponding model in Supplementary Fig. 15d and blue curve in Supplementary Fig. 15c).

Due to the versatility of the L-PBF technique, further property optimization is possible, for example, by tuning individual layer microstructure via different laser parameters and/or scan strategies. The approach could also potentially build materials with other functional properties in addition to high strength and high ductility. Note that the elemental segregations observed in the Concept samples might not be beneficial for corrosion resistance purposes[18]. Further flaw elimination in L-PBF metals remains a current challenge, but is expected to continue improving the

materials properties beyond those achievable through conventional processing approaches. Nevertheless, our work here demonstrates a new class of 3D-printed 316L SS that exhibits an exceptional combination of strength and ductility well surpassing that of conventional counterparts. These superior properties arise from the collective effects of hierarchically heterogeneous microstructures, including solidification cellular structure, LAGBs, and dislocations. This work demonstrates the flexibility of the AM technique to tailor microstructures and produce metals and alloys with excellent properties.

Methods

Methods, including statements of data availability and any associated accession codes and references, are available in the online version of this paper.

Received 2 May 2017; accepted 29 September 2017; published online 30 October 2017

References

1. Li, Z., Pradeep, K. G., Deng, Y., Raabe, D. & Tasan, C. C. Metastable high-entropy dual-phase alloys overcome the strength–ductility trade-off. *Nature* **534,** 227–230 (2016).
2. Kimura, Y., Inoue, T., Yin, F. & Tsuzaki, K. Inverse temperature dependence of toughness in an ultrafine grain-structure steel. *Science* **320,** 1057–1060 (2008).
3. Yamamoto, Y. *et al*. Creep-resistant, Al_2O_3-forming austenitic stainless steels. *Science* **316,** 433–436 (2007).
4. Eoyama, M. *et al*. Bone-like crack resistance in hierarchical metastable nanolaminate steels. *Science* **355,** 1055–1057 (2017).
5. Gludovatz, B. *et al*. A fracture-resistant high-entropy alloy for cryogenic applications. *Science* **345,** 1153–1158 (2014).
6. Hofmann, D. C. *et al*. Designing metallic glass matrix composites with high toughness and tensile ductility. *Nature* **451,** 1085–1089 (2008).
7. Kim, S.-H., Kim, H. & Kim, N. J. Brittle intermetallic compound makes ultrastrong low-density steel with large ductility. *Nature* **518,** 77–79 (2015).
8. Jiang, S. *et al*. Ultrastrong steel via minimal lattice misfit and high-density nanoprecipitation. *Nature* **544,** 460–464 (2017).
9. Wang, Y. M., Chen, M. W., Zhou, F. H. & Ma, E. High tensile ductility in a nanostructured metal. *Nature* **419,** 912–915 (2002).
10. Fang, T. H., Li, W. L., Tao, N. R. & Lu, K. Revealing extraordinary intrinsic tensile plasticity in gradient nano-grained copper. *Science* **331,** 1587–1590 (2011).
11. Yan, F. K., Liu, G. Z., Tao, N. R. & Lu, K. Strength and ductility of 316L austenitic stainless steel strengthened by nano-scale twin bundles. *Acta Mater.* **60,** 1059–1071 (2012).
12. Wei, Y. *et al*. Evading the strength- ductility trade-off dilemma in steel through gradient hierarchical nanotwins. *Nat. Commun.* **5,** 3580 (2014).
13. Wu, X. L. *et al*. Heterogeneous lamella structure unites ultrafine-grain strength with coarse-grain ductility. *Proc. Natl Acad. Sci. USA* **112,** 14501–14505 (2015).
14. Herzog, D., Seyda, V., Wycisk, E. & Emmelmann, C. Additive manufacturing of metals. *Acta Mater.* **117,** 371–392 (2016).
15. MacDonald, E. & Wicker, R. Multiprocess 3D printing for increasing component functionality. *Science* **353,** 1512 (2016).
16. Khairallah, S. A., Anderson, A. T., Rubenchik, A. & King, W. E. Laser powder-bed fusion additive manufacturing: physics of complex melt flow and formation mechanisms of pores, spatter, and denudation zones. *Acta Mater.* **108,** 36–45 (2016).
17. Kamath, C., El-dasher, B., Gallegos, G. F., King, W. E. & Sisto, A. Density of additively-manufactured, 316L SS parts using laser powder-bed fusion at powers up to 400 W. *Int. J. Adv. Manuf. Technol.* **74,** 65–78 (2014).
18. Trelewicz, J. R., Halada, G. P., Donaldson, O. K. & Manogharan, G. Microstructure and corrosion resistance of laser additively manufactured 316L stainless steel. *J. Miner. Metals Mater. Soc.* **68,** 850–859 (2016).
19. Prashanth, K. G. & Eckert, J. Formation of metastable cellular microstructures in selective laser melted alloys. *J. Alloys Compd* **707,** 27–34 (2017).
20. Ion, J. C., Shercliff, H. R. & Ashby, M. F. Diagrams for laser materials processing. *Acta Metall. Mater.* **40,** 1539–1551 (1992).
21. Thomas, M., Baxter, G. J. & Todd, I. Normalised model-based processing diagrams for additive layer manufacture of engineering alloys. *Acta Mater.* **108,** 26–35 (2016).
22. Rawers, J., Croydon, F., Krabbe, R. & Duttlinger, N. Tensile characteristics of nitrogen enhanced powder injection moulded 316L stainless steel. *Powder Metall.* **39,** 125–129 (1996).
23. Zieliński, W., Abduluyahed, A. A. & Kurzydłowski, K. J. TEM studies of dislocation substructure in 316 austenitic stainless steel strained after annealing in various environments. *Mater. Sci. Eng. A* **249,** 91–96 (1998).
24. Nakanishi, T., Tsuchiyama, T., Mitsuyasu, H., Iwamoto, Y. & Takaki, S. Effect of partial solution nitriding on mechanical properties and corrosion resistance in a type 316L austenitic stainless steel plate. *Mater. Sci. Eng. A* **460–461,** 186–194 (2007).
25. Liu, G. Z., Tao, N. R. & Lu, K. 316L austenite stainless steels strengthened by means of nano-scale twins. *J. Mater. Sci. Technol.* **26,** 289–292 (2010).
26. Ravi Kumar, B., Sharma, S. & Mahato, B. Formation of ultrafine grained microstructure in the austenitic stainless steel and its impact on tensile properties. *Mater. Sci. Eng. A* **528,** 2209–2216 (2011).
27. Ueno, H., Kakihata, K., Kaneko, Y., Hashimoto, S. & Vinogradov, A. Enhanced fatigue properties of nanostructured austenitic SUS 316L stainless steel. *Acta Mater.* **59,** 7060–7069 (2011).
28. Lu, K., Yan, F. K., Wang, H. T. & Tao, N. R. Strengthening austenitic steels by using nanotwinned austenitic grains. *Scr. Mater.* **66,** 878–883 (2012).
29. Albertini, C., Cadoni, E. & Solomos, G. Advances in the Hopkinson bar testing of irradiated/non-irradiated nuclear materials and large specimens. *Phil. Trans. R. Soc. A* **372,** 20130197 (2014).
30. Mower, T. M. & Long, M. J. Mechanical behavior of additive manufactured, powder-bed laser-fused materials. *Mater. Sci. Eng. A* **651,** 198–213 (2016).
31. Chen, X. H., Lu, J., Lu, L. & Lu, K. Tensile properties of a nanocrystalline 316L austenitic stainless steel. *Scr. Mater.* **52,** 1039–1044 (2005).
32. Kumar, B. R., Sharma, S. & Mahato, B. Formation of ultrafine grained microstructure in the austenitic stainless steel and its impact on tensile properties. *Mater. Sci. Eng. A* **528,** 2209–2216 (2011).
33. Fernandes de Lima, M. S. & Sankare, S. Microstructure and mechanical behavior of laser additive manufactured AISI 316 stainless steel stringers. *Mater. Des.* **55,** 526–532 (2014).
34. Saeidi, K., Gao, X., Zhong, Y. & Shen, Z. J. Hardened austenite steel with columnar sub-grain structure formed by laser melting. *Mater. Sci. Eng. A* **625,** 221–229 (2015).
35. Wang, D., Song, C. H., Yang, Y. Q. & Bai, Y. C. Investigation of crystal growth mechanism during selective laser melting and mechanical property characterization of 316L stainless steel parts. *Mater. Des.* **100,** 291–299 (2016).
36. Zhang, K., Wang, S., Liu, W. & Shang, X. Characterization of stainless steel parts by laser metal deposition shaping. *Mater. Des.* **55,** 104–119 (2014).
37. Mertens, A. *et al*. Mechanical properties of alloy Ti–6Al–4V and of stainless steel 316L processed by selective laser melting: influence of out-of-equilibrium microstructures. *Powder Metall.* **57,** 184–189 (2014).
38. Amato, K. N. *et al*. Microstructures and mechanical behavior of Inconel 718 fabricated by selective laser melting. *Acta Mater.* **60,** 2229–2239 (2012).
39. Gu, D. *et al*. Densification behavior, microstructure evolution, and wear performance of selective laser melting processed commercially pure titanium. *Acta Mater.* **60,** 3849–3860 (2012).
40. Vrancken, B., Thijs, L., Kruth, J. P. & Van Humbeeck, J. Microstructure and mechanical properties of a novel beta titanium metallic composite by selective laser melting. *Acta Mater.* **68,** 150–158 (2014).
41. Saeidi, K., Kvetkova, L., Lofajc, F. & Shen, Z. Austenitic stainless steel strengthened by the *in situ* formation of oxide nanoinclusions. *Rsc Adv.* **5,** 20747–20750 (2015).
42. Tolosa, I., Garciandia, F., Zubiri, F., Zapirain, F. & Esnaola, A. Study of mechanical properties of AISI 316 stainless steel processed by 'selective laser melting', following different manufacturing strategies. *Int. J. Adv. Manuf. Technol.* **51,** 639–647 (2010).
43. Sun, Z., Tan, X., Tor, S. B. & Yeong, W. Y. Selective laser melting of stainless steel 316L with low porosity and high build rates. *Mater. Des.* **104,** 197–204 (2016).
44. Zhong, Y., Liu, L. F., Wikman, S., Cui, D. Q. & Shen, Z. J. Intragranular cellular segregation network structure strengthening 316L stainless steel prepared by selective laser melting. *J. Nucl. Mater.* **470,** 170–178 (2016).
45. Murr, L. E. *et al*. Metal fabrication by additive manufacturing using laser and electron beam melting technologies. *J. Mater. Sci. Technol.* **28,** 1–14 (2012).
46. Wu, J., Wang, X. Q., Wang, W., Attallah, M. M. & Loretto, M. H. Microstructure and strength of selectively laser melted $AlSi_{10}Mg$. *Acta Mater.* **117,** 311–320 (2016).
47. Tomota, Y., Lukas, P., Neov, D., Harjo, S. & Abe, Y. R. *In situ* neutron diffraction during tensile deformation of a ferrite-cementite steel. *Acta Mater.* **51,** 805–817 (2003).
48. Clausen, B., Lorentzen, T. & Leffers, T. Self-consistent modelling of the plastic deformation of FCC polycrystals and its implications for diffraction measurements of internal stresses. *Acta Mater.* **46,** 3087–3098 (1998).
49. Yan, K., Carr, D. G., Callaghan, M. D., Liss, K.-D. & Li, H. Deformation mechanisms of twinning-induced plasticity steels: *in situ* synchrotron characterization and modeling. *Scr. Mater.* **62,** 246–249 (2010).

50. Mughrabi, H. Deformation-induced long-range internal stresses and lattice plane misorientations and the role of geometrically necessary dislocations. *Philos. Mag.* **86,** 4037–4054 (2006).

Acknowledgements

The authors thank S. Khairallah, T. Haxhimali, G. Guss, S. Burke, P. Alexander, B. El-dasher, W. King and C. Kamash for their experimental assistance and/or inspiring discussion. J. Li is acknowledged for his initial contribution to the model set-up. R.T.O. acknowledges support from the US Department of Energy, Basic Energy Sciences, Materials Science and Engineering Division, under Contract No. DEAC02-07CH11358. This work was performed under the auspices of the US Department of Energy by Lawrence Livermore National Laboratory under contract No. DE-AC52-07NA27344. ChemiSTEM was performed at the OSU Electron Microscope Facility which is supported by NSF MRI grant number 1040588 and by the Murdock Charitable Trust and the Oregon Nanoscience and Micro-Technologies Institute. This research used resources of the Advanced Photon Source, a US Department of Energy (DOE) Office of Science User Facility operated for the DOE Office of Science by Argonne National Laboratory under Contract No. DE-AC02-06CH11357.

Author contributions

Y.M.W., T.V., J.T.M., T.T.R. and M.K.S. characterized microstructures. T.V., J.Y., W.C. and Z.L. performed mechanical testing. Y.M.W., J.Y., N.P.C. and R.T.O. conducted *in situ* SXRD experiments and analysed the resultant data. P.J.D. and M.J.M. were involved with processing parameter development and sample print. Z.Z., Y.Z. and T.Z. constructed the models and conducted simulations. Y.M.W., T.V. and T.Z. drafted the initial manuscript. Y.M.W. conceived, designed, and led the project. All co-authors contributed to the data analysis and discussion.

Additional information

Supplementary information is available in the online version of the paper. Reprints and permissions information is available online at www.nature.com/reprints. Publisher's note: Springer Nature remains neutral with regard to jurisdictional claims in published maps and institutional affiliations. Correspondence and requests for materials should be addressed to Y.M.W.

Competing financial interests

The authors declare no competing financial interests.

Methods

Materials fabrication and mechanical tests. The first type of 316L SS samples used in this study were fabricated by a commercial Concept Laser M2 powder-bed-fusion (L-PBF) machine equipped with a 400-W fibre laser in an argon environment. The beam size is 54 μm. This set of samples is referred to as 'Concept samples'. The oxygen content was maintained below ~0.1–0.2% during L-PBF processing, and the build plate was 304 SS. A plasma-atomized 316L powder was used (Additive Metal Alloys (AMA)), with a mean particle size of ~30 μm. To obtain near fully dense samples, we performed a series of control experiments by building 316L SS pillars (10 mm (length) × 10 mm (width) × 8 mm (height)) and applied a density optimization approach to optimizing the laser parameters[17]. Microstructure and mechanical property characterizations were conducted on selected pillar samples, including nanoindentation and compression tests. For tensile plate builds (40 mm (length) × 20 mm (width) × 2 mm (thickness)), we chose laser parameters that yielded samples with a density better than 99.2%. Both continuous and island scan strategies were applied. Dogbone samples with a gauge section of 6.5 mm (length) × 1.5 mm (width) × 1.1 mm (thickness) were machined from the build plates for tensile tests. Two 3.5 mm gauge length samples were also machined for comparison purpose. Before the test, all samples were polished down to a metallurgical grit of 1200 SiC paper.

The second type of 316L SS samples were built using an open architecture Fraunhofer L-PBF machine, with a 207 μm beam diameter. This batch of samples is referred to as 'Fraunhofer samples'. The machine uses a 400-W fibre laser and an argon build environment. Eighteen thin plates (40 mm (length) × 40 mm (width) × 3 mm (thickness)) were built with a 316L SS powder similar to that used by the Concept machine. Plates were built both horizontally and vertically, with 90° or 45° hatching patterns. A continuous scan strategy was adopted for these plates. The same geometry tensile samples as those from the Concept builds were machined out of these plates.

Uniaxial tensile tests were carried out in an Instron 4444 tensile machine at a nominal strain rate range of 1×10^{-4} s^{-1}–1×10^{-3} s^{-1}. The load cell has a maximum capacity of 2 kN. The tensile elongation was measured by an LE-01 laser extensometer (Electronic Instrument Research) with a displacement resolution of 1 μm. Two pieces of silver tape were attached to the sample gauge and act as reflective markers for the laser extensometer. The tests were repeated two to three times for each type of sample, which yielded standard error bars.

Composition analysis. The compositions of L-PBF 316L steels were analysed by inductively coupled plasma mass spectroscopy (ICP-MS) for metallic elements and instrumental gas analysis (IGA) for light elements (for example, oxygen, nitrogen, hydrogen) (Evans Analytical Group, LLC.), after dust and moisture removal. The details of the IGA method can found in ref. 51.

Synchrotron X-ray diffraction (SXRD). Standard diffraction data were collected at the Advanced Photon Source (APS) of Argonne National Laboratory at beamline 11-ID-B, equipped with an amorphous silicon-based area detector (Perkin-Elmer). The X-ray beam energy was 86.70 keV ($\lambda=0.1430$ Å), and the beam size was 0.5×0.5 mm^2. The sample to detector distance was set at 95 cm.

In situ SXRD tensile tests were conducted at beamline 6-ID-D at APS. Two-dimensional (2D) X-ray diffraction patterns were collected in transmission mode at the gauge section of the dogbone tensile specimen (gauge length: 8.0 mm, width: 1.5 mm, thickness: 0.5 mm) with monochromatic, 100.135 keV ($\lambda=0.123595$ Å) X-rays and a slit size of 1 mm (width) × 0.2 mm (height). Diffraction data were collected in transmission geometry using a GE amorphous silicon detector with a 200×200 μm^2 pixel size that is positioned at 142.4 cm behind the sample. Diffraction patterns were collected every 2 s in real time during uniaxial tensile deformation. The samples were loaded with a Zwicki Z2.5 tester equipped with a non-contact laser extensometer to measure the strain. The nominal strain rate was ~$2.0–4.0\times10^{-4}$ s^{-1}. The diffraction patterns were integrated in 8° azimuthal bins using Fit2D to obtain 1D diffraction patterns as a function of the azimuthal angle. To quantify the elastic lattice strain, inhomogeneous strain (peak broadening), and texture changes during loading, the peaks in the 1D patterns were fitted with a pseudo-Voigt function using a custom Matlab program. The stress-free reference 316L sample was obtained by annealing an as-printed Concept sample at 1,038 °C for 1 h followed by furnace cooling under an argon environment. A separate reference sample annealed at 1,200 °C for 1 h was also used for comparison. The selection of the reference materials affects the absolute elastic lattice strain values but not the general trends observed in Fig. 3.

Electron backscatter diffraction (EBSD) in a scanning electron microscope (SEM). EBSD was performed in a Quanta 200 Field Emission Gun SEM (FEG/SEM) equipped with a four-quadrant solid-state backscatter electron detector. A TexSEM Laboratories OIM 4 system equipped with a Peltier-cooled charge-coupled device camera was used. Specimens were tilted to 70° in the SEM chamber at an accelerating voltage of 30 keV. A typical scan area of 2 mm × 2 mm was used for EBSD analysis with a step size of 0.1–1 μm. EBSD data were analysed with the Orientation Imaging Microscopy (OIM) Analysis software provided by EDAX. To calculate the grain size, each grain was considered as a sphere from which the diameter (grain size) was deducted. Interfaces between grains were considered as low-angle grain boundaries (LAGBs) when the misorientation angle was 2°–10°, otherwise they were considered as high-angle grain boundaries (HAGBs).

Transmission electron microscopy (TEM) and inverse-pole figure orientation mapping (IPFOM) in TEM. Conventional bright-field (BF), dark-field (DF), and high-angle annular dark-field (HAADF) TEM were performed in a FEI 80-300 Titan TEM operated at 300 kV with a point-to-point resolution of ≤0.2 nm and a maximum resolution of ≤0.135 in HAADF high-resolution STEM mode. The IPFOM was performed in a Philips CM-300 microscope operated at 300 kV. The resolution of the IPFOM depends on the probe size and the scan step size. Similar IPFOM techniques have been used previously in our work to identify nanometre-scale defects on coherent twin boundaries[52]. The chemical mapping was performed using an FEI Titan TEM at Oregon State University, with ChemiSTEM capability, to generate high-quality STEM energy-dispersive X-ray spectroscopy (EDS) maps using its four embedded Bruker SDD detectors and an accelerating voltage of 200 kV. TEM samples were prepared by standard electropolishing techniques.

The construction of the normalized processing diagram for L-PBF 316L SS. To compare various laser processing parameters used in this work, we follow the pioneering work of Ion *et al.*[20] and Thomas *et al.*[21] to calculate various parameters as follows:

$$E^*_{\min}=\frac{p^*}{v^*l^*}=\frac{Ap}{2vlr_b\rho C_p(T_m-T_0)} \tag{1}$$

where $E^*_{\min}$ is the dimensionless normalized volumetric energy density required to melt the material, and P^*, v^*, and l^* are the dimensionless normalized laser power, laser speed, and layer thickness, respectively. A is the surface absorptivity (~0.35) (ref. 16), p the laser power (W), v the laser speed (m s^{-1}), l the layer thickness (m), r_b the beam radius (m), ρ the density of 316L SS (kg m^{-3}), C_p the specific heat capacity (J kg^{-1} K^{-1}), T_m the melting temperature (1,673 K), and T_0 the initial (or powder bed) temperature (K). For both Concept and Fraunhofer machines, the beam spot size is defined by D4σ values.

The dimensionless beam power is defined as follows:

$$p^*=\frac{Ap}{r_bk(T_m-T_0)} \tag{2}$$

where k, the thermal conductivity, is given by:

$$k=14.307+0.0181T_m-6\times10^{-6}T_m^2 \tag{3}$$

The dimensionless beam speed is obtained hereafter:

$$v^*=\frac{vr_b}{D} \tag{4}$$

where D is the thermal diffusivity at melting (5.38×10^{-6} m^2 s^{-1}) (ref. 53).

The dimensionless layer thickness is calculated as

$$l^*=\frac{2l}{r_b} \tag{5}$$

The dimensionless hatch spacing (h^*) is

$$h^*=\frac{h}{r_b} \tag{6}$$

where h is the hatch spacing.

Estimate of the oxide strengthening effect. Assuming oxides observed in L-PBF 316L SS act as the pinning obstacles to dislocation motion and using the Orowan strengthening model, we evaluate the contribution to strength due to nanoparticles according to

$$\tau=Gb/(L-d) \tag{7}$$

where G (=78 GPa) is the shear modulus of 316L SS, b (=0.258 nm) the Burgers vector. L the average distance between particles, and d the average

diameter of particles. The particles measured in a Concept sample have an average distance and spacing of $L = 4.1\,\mu m$ and $d = 65$ nm (see Supplementary Fig. 9), respectively. This yields a strengthening effect of $\tau = 5$–10 MPa, which is negligibly small.

Crystal plasticity finite element modelling. *Grain-size-dependent crystal plasticity model.* To investigate the effect of grain-size distribution on the stress–strain behaviour of L-PBF 316L SS, the conventional crystal plasticity theory was extended by incorporating the grain-size dependence of yield strength[54–57]. The complete details of the grain-size-dependent crystal plasticity model used in this work can be found in a recent article by Zeng and colleagues[54]. To apply this model to L-PBF 316L SS, we assumed the slip resistance parameters in each grain, including $\{s_0, h_0, a, s_{sat}, m\}$, were inversely proportional to the square root of grain size d,

$$\{s_0(d), h_0(d), a(d), s_{sat}(d), m(d)\} \sim d^{-1/2} \tag{8}$$

In equation (8), the initial slip resistances s_0 were estimated from the Hall–Petch relation given in the main text, $\sigma_y = 183.31 + 253.66/\sqrt{d}$ (MPa) (by using the Taylor factor of 2.5) (ref. 10). The strain rate sensitivity m of coarse-grained (CG) SS varied from 0.007 to 0.005 for grain size d from 3.1 to 33 μm (refs 58,59). The strain-hardening-related parameters $\{h_0, a, s_{sat}\}$ were determined by fitting to the experimental stress–strain curves of SS for two grain sizes of 3.1 μm and 33 μm (ref. 60). For the 3.1 μm grain, we took $h_0 = 980$ MPa, $a = 3.2$, $s_{sat} = 1{,}050$ MPa; and for the 33 μm grain, $h_0 = 1{,}030$ MPa, $a = 3.5$, $s_{sat} = 950$ MPa. To evaluate $\{h_0, a, s_{sat}, m\}$ for intermediate grain sizes, we used the above bounding values to fit the formula of $A = B + C \cdot d^{-1/2}$, where B and C are the fitting constants. The following fitting formulae were obtained:

$$s_0\ (\mathrm{MPa}) = 73.32 + 101.46 d^{-1/2}, \quad h_0\ (\mathrm{MPa}) = 1{,}052.1 - 126.94 d^{-1/2} \tag{9}$$

$$a = 3.6326 - 0.7616 d^{-1/2}, \quad s_{sat}\ (\mathrm{MPa}) = 905.8 + 253.88 d^{-1/2}$$

$$m = 0.0041 + 0.0051 d^{-1/2}$$

Other material properties, including elastic constants (C_{11}, C_{12}, C_{44}), twelve $\{111\}\langle 110\rangle$ slip systems, and the latent hardening matrix $\{q^{\alpha\beta}\}$, were assumed to be independent of grain size. For face-centred cubic Fe, we took $C_{11} = 260$ GPa, $C_{12} = 111$ GPa and $C_{44} = 77$ GPa; $q^{\alpha\beta} = 1.0$ if the slip systems α and β are coplanar and $q^{\alpha\beta} = 1.4$ if they are non-coplanar[57].

Finite element model and simulation. Supplementary Fig. 15a shows a three-dimensional polycrystal model of L-PBF SS created with the open-source software Neper[61]. The grain sizes in this model are widely distributed so as to match the experimental measurements of the grain volume distribution (Supplementary Fig. 15b). To construct the model, the first step was to pack poly-dispersed spherical particles with a prescribed distribution of diameters. The geometry of packed particles was generated from a discrete element method simulation with LAMMPS[62,63]. In this simulation, spherical particles with diameters ranging from 3 to 30 μm were poured into a cubic container. The number of particles with each diameter was prescribed. The built-in Hertzian model for granular spherical particles was used to simulate the particle interactions, and the particle system was relaxed[64–66]. After relaxation, the centroids of the particles were taken as the centroids of the grains, and the diameters of the particles as the grain diameters. Given the diameter and the centroid coordinate of each particle, Laguerre tessellation was applied to construct the weighted Voronoi diagram with Neper. Each Voronoi cell is a polyhedron with an irregular shape, representing a grain in the L-PBF SS structure. The diameter and the volume of each grain were calculated with the built-in functions in Neper. Furthermore, the fractions of particles with different diameters were carefully tuned to obtain the desired volume fraction in Supplementary Fig. 15b. Then the polycrystal structure was meshed with the built-in meshing function in Neper with four-node linear tetrahedral elements (C3D4). The meshes were imported into ABAQUS/CAE to reproduce the sample of the L-PBF SS in ABAQUS/CAE[67]. The overall sample geometry is $73\,\mu m \times 73\,\mu m \times 73\,\mu m$ ($x \times y \times z$) with a total of 88,944 elements. Displacements and tractions are continuous at grain boundaries, such that no separation or sliding is allowed between any pair of adjoining grains.

Using the finite element structure model of L-PBF SS in Supplementary Fig. 15a, we performed the grain-size-dependent crystal plasticity simulations of uniaxial compression of L-PBF 316L SS. We used an experimental compression curve, as it better represents the intrinsic strain-hardening behaviour of L-PBF SS. The orientation of grains was assigned randomly in terms of three Euler angles, $\{\theta, \varphi, \Omega\}$, representing rotations from the crystal basis to the global basis[57]. A user material subroutine VUMAT was developed in ABAQUS/EXPLICIT to implement the grain-size-dependent crystal plasticity model described above. With reference to Supplementary Fig. 15a, the boundary conditions of the L-PBF SS sample were prescribed as follows: on the $x = 0$ surface, the displacement in the x direction is zero ($u_x = 0$); on the $y = 0$ surface, the displacement in the y direction is zero ($u_y = 0$); on the $z = 0$ surface, the displacement in the z direction is zero ($u_z = 0$); on the $y = 73\,\mu m$ and $z = 73\,\mu m$ surfaces, the traction is zero; on the $x = 73\,\mu m$ surface, the velocity in the x direction is constant ($v_x = -7.3 \times 10^{-4}\,\mu m\,s^{-1}$), corresponding to an applied compressive strain rate of $10^{-5}\,s^{-1}$. In Supplementary Fig. 15c, we compare the experimental measurement (black curve) and the simulation result (green curve) from the polycrystal model with a wide distribution of grain sizes. The large discrepancy indicates that the subgrain heterogeneities and defects play a dominant role in governing the strength and hardening of L-PBF SS.

To estimate the effective strength-controlling length scale associated with subgrain heterogeneities and defects, we assumed, to a first approximation, that the slip resistance parameters are governed by a single subgrain length L. By fitting to the experimental stress–strain curve of L-PBF SS, we obtained the slip resistance parameters: $s_0 = 300$ MPa, $h_0 = 320$ MPa, $a = 1.1$, $s_{sat} = 980$ MPa. The strain rate sensitivity m is 0.025, which was measured in our experiments. To match the Hall–Petch relation of yield strength,

$$\sigma_y = 183.31 + 253.66/\sqrt{L}\,(\mathrm{MPa}) \tag{10}$$

the corresponding L was estimated as ~205 nm. This indicates that the effective strength-controlling length scale is much smaller than the average size of subgrain cellular structures, which was measured to be in the range of 300–1,000 nm in our experiments.

In fact, our experiments showed that the grains containing subgrain cellular structures typically occupy ~40–70% volume fraction of the sample. To investigate the effects of subgrain cellular structures on the stress–strain behaviour of the entire sample, we randomly selected 60% grains in the finite element polycrystal model as the grains containing cellular structures. Supplementary Fig. 15d shows a mixture model containing the grains without cellular structures (coloured in green) and grains with cellular structures (coloured in red), the latter of which occupy ~60% volume fraction of the sample. The constitutive relation in the former depends on grain size, and thus obeys the Hall–Petch relation of equation (9). In contrast, the constitutive relation in the latter is controlled by a single subgrain length scale $L = 205$ nm, and thus obeys equation (10). The simulated stress–stress curve from this model is shown in Supplementary Fig. 15c as the blue curve, which is markedly different from the experimental measurement. This result indicates that the strength and hardening of L-PBF SS are not controlled by a single length scale associated with the subgrain cellular structures. Instead, a multitude of structural and chemical heterogeneities, including HAGBs, LAGBs, subgrain cellular structures, sub-cell dislocations, and segregated elements, collectively give rise to high yield strength as well as an exceptional combination of strength, hardening and tensile ductility.

Data availability. The data that support the findings of this study are available from the corresponding author on reasonable request.

References

51. Wang, Y. M. *et al*. Controlling factors in tensile deformation of nanocrystalline cobalt and nickel. *Phys. Rev. B* **85,** 014101 (2012).
52. Wang, Y. M. *et al*. Defective twin boundaries in nanotwinned metals. *Nat. Mater.* **12,** 697–702 (2013).
53. King, W. E. *et al*. Observation of keyhole-mode laser melting in laser powder-bed fusion additive manufacturing. *J. Mater. Process. Technol.* **214,** 2915–2925 (2014).
54. Zeng, Z. *et al*. Gradient plasticity in graident nano-grained metals. *Extreme Mech. Lett.* **8,** 213–219 (2016).
55. Rice, J. R. Inelastic constitutive relations for solids: an internal-variable theory and its application to metal plasticity. *J. Mech. Phys. Solids* **19,** 433–455 (1971).
56. Asaro, R. J. & Rice, J. R. Strain localization in ductile single crystals. *J. Mech. Phys. Solids* **25,** 309–338 (1977).
57. Kalidindi, S. R., Bronkhorst, C. A. & Anand, L. Crystallographic texture evolution in bulk deformation processing of FCC metals. *J. Mech. Phys. Solids* **40,** 537–569 (1992).
58. Jang, D. & Atzmon, M. Grain-boundary relaxation and its effect on plasticity in nanocrystalline Fe. *J. Appl. Phys.* **99,** 083504 (2006).
59. Rodrguez-Baracaldo, R., Benito, J. A., Caro, J., Cabrera, J. M. & Prado, J. M. Strain rate sensitivity of nanocrystalline and ultrafine-grained steel obtained by mechanical attrition. *Mater. Sci. Eng. A* **485,** 325–333 (2008).
60. Kashyap, B. P. & Tangri, K. On the Hall–Petch relationship and substructural evolution in type 316L stainless steel. *Acta Metall. Mater.* **43,** 3971–3981 (1995).

61. Quey, R., Dawson, P. R. & Barbe, F. Large-scale 3D random polycrystals for the finite element method: generation, meshing and remeshing. *Comput. Methods Appl. Mech. Eng.* **200,** 1729–1745 (2011).
62. Plimpton, S. & Hendrickson, B. A new parallel method for molecular dynamics simulation of macromolecular systems. *J. Comput. Chem.* **17,** 326–337 (1996).
63. Radjaï, F. & Dubois, F. *Discrete-Element Modeling of Granular Materials* (Wiley-ISTE, 2011).
64. Brilliantov, N. V., Spahn, F., Hertzsch, J.-M. & Pöschel, T. Model for collisions in granular gases. *Phys. Rev. E* **53,** 5382–5392 (1996).
65. Silbert, L. E. *et al*. Granular flow down an inclined plane: Bagnold scaling and rheology. *Phys. Rev. E* **64,** 051302 (2001).
66. Zhang, H. P. & Makse, H. A. Jamming transition in emulsions and granular materials. *Phys. Rev. E* **72,** 011301 (2005).
67. Abaqus, *Abaqus 6.13 Documentation* (Dassault Systèmes, 2013).